

Convolutional Neural Network Combined With Stochastic Parallel Gradient Descent to Decompose Fiber Modes Based on Far-Field Measurements

Byungho Kim , Jeongkyun Na , and Yoonchan Jeong , *Member, IEEE*

Abstract—Modal decomposition (MD) of fiber modes based on direct far-field measurement combining the convolutional neural network (CNN) with a stochastic parallel gradient descent (SPGD) algorithm is investigated both numerically and experimentally. For obtaining the modal coefficients of fiber modes guided in a large-mode-area fiber, the fiber modes are decomposed into a finite number of Hermite gaussian modes, the initial conditions of the modal coefficients are obtained through the CNN, and further optimization of them are carried out through the SPGD. The ambiguity problem that may happen in the CNN owing to the existence of the pair-beam field is resolved by properly labelling the phase differences with a single-valued parameter set in consideration of the mode-order indices. The feasibility and effectiveness of the proposed MD method is verified both numerical simulations and experimental demonstrations with both recorded image data and online real-time image data. The correlation error incurred by the proposed method is below 6.6×10^{-4} and 8.7×10^{-3} in the numerical simulations and the experimental demonstrations, respectively. The online real-time operation of the proposed method is also experimentally demonstrated at a decomposing rate of ~ 2 Hz.

Index Terms—Convolutional neural network, deep learning, modal decomposition, multimode fiber, stochastic parallel gradient descent.

I. INTRODUCTION

SINCE a multi-mode fiber (MMF) or a large-mode-area fiber (LMAF) has the advantage of high energy capacity thanks to its large mode area in comparison with that of a single-mode fiber (SMF), the interest in the use of an MMF/LMAF in the field of high-power fiber lasers has been growing [1], [2], besides its conventional applications to fiber imaging and short-distance communications [3], [4]. Although its use

Manuscript received 20 December 2022; revised 1 May 2023; accepted 6 May 2023. Date of publication 16 May 2023; date of current version 19 September 2023. This work was supported by the ADD of South Korea under Grant UD210019ID. (*Corresponding author: Yoonchan Jeong.*)

This work did not involve human subjects or animals in its research.

Byungho Kim and Jeongkyun Na are with the Department of Electrical and Computer Engineering, Seoul National University, Seoul 06288, South Korea (e-mail: kimbh5057@snu.ac.kr; najk8821@snu.ac.kr).

Yoonchan Jeong is with the Department of Electrical and Computer Engineering, Seoul National University, Seoul 06288, South Korea, and also with the ISRC and IAP, Seoul National University, Seoul 08826, South Korea (e-mail: yoonchan@snu.ac.kr).

Color versions of one or more figures in this article are available at <https://doi.org/10.1109/JLT.2023.3276366>.

Digital Object Identifier 10.1109/JLT.2023.3276366

is in the limelight in various applications, there are drawbacks that unwanted higher-order modes (HOMs) tend to be excited due to transverse mode instability or mode coupling [5], [6]. To confront the abovementioned issues, the quantitative analysis of HOMs must be preceded. On this account, the modal decomposition (MD) method that can reliably and swiftly analyze the modal fraction and the phases of the modes excited in the given MMF/LMAF is more and more in demand [7], [8], [9], [10], [11], [12], [13], [14], [15], [16], [17], [18], [19], [20], [21], [22], [23], [24]. For decomposing HOMs in an MMF/LMAF, various MD methods have been investigated, which were more or less based on the stochastic parallel gradient descent (SPGD) algorithm [9], [10], [11], [12], [13], the genetic algorithm [14], the analytic calculation [15], [16], and the convolutional neural network (CNN) [17], [18], [19], [20], [21], [22], [23], [24]. Although such a variety of MD methods have been looked into, most previous studies utilized a scheme under which fiber modes were decomposed based on the near-field intensity patterns of them [10], [11], [12], [15], [16], [17], [18], [19], [20]. In general, a charge-coupled device (CCD) camera is used to obtain the intensity pattern. However, it is not straightforward to obtain a near-field intensity pattern with a CCD with a high resolution, because the core diameter of an ordinary MMF/LMAF is normally less than several tens of micrometers. For resolving this resolution issue, it is common to obtain images with a CCD camera by magnifying the size of the near-field intensity pattern via installing an additional optical system, such as a 4-f system [10], [11], [12], [15], [16], [17], [18], [19], [20]. However, the use of an additional optical system complicates the MD procedure, also causing unwanted beam distortion by lens aberration, misalignment of optics, etc., which can lower the overall accuracy of the resultant MD [25].

To overcome the resolution issue of the MD methods by means of the measurement of near-field intensity patterns, we have recently proposed an SPGD-based MD method by means of the direct measurement of far-field intensity patterns [9] without relying on an additional 4-f system, successfully demonstrating the MD with high accuracy as well as having no considerable issues aforementioned. Moreover, the proposed MD method could take much less time than the previous ones [14], because it could decompose the far-field intensity pattern into the free-space Hermite-Gaussian-modes (HGMS) without going through any auxiliary numerical calculations, such as Fourier

transforms [9], [26], [27]. Moreover, to confront the uniqueness issue, which is similar to the conjugation-pair issue of most near-field MD methods, we carried out the measurement of the far-field intensity pattern at two different distances and could successfully achieve a unique modal solution [9].

Whilst the aforementioned scheme could yield high-accuracy outcomes, the numerical method, i.e., the SPGD-based numerical procedure itself had an inherent limitation in terms of the capability to provide real-time MD data when compared with other MD methods based on the CNN and the analytic calculation [15], [20]. For example, it has been reported that in a 3-mode case, the MD rates achievable from the CNN and the analytic calculation methods could go over tens of kHz [10], [15], [20], which are, in fact, three-order of magnitude faster than those by the SPGD-based numerical methods, although the MD methods by the CNN and the analytic calculation are not free from drawbacks in that the correlation accuracy of them can degrade substantially when carried out in realistic or non-ideal measurement conditions [9], [11], [15], [16], [18], [20]. In addition, the SPGD-based numerical procedure has another limitation that it may take excessive time or need special measures to escape from local minima when initially ill-conditioned with a non-convex loss function [9], [10], [11].

Recently, a novel MD method combining the advantage of the SPGD algorithm in terms of accuracy and the advantage of CNN in terms of speed has been proposed based on numerical simulations [28]. It was reported that this method could overcome the typical local-minimum issue of the SPGD algorithm by first obtaining the interim conditions close to the global minimum via the CNN and could greatly reduce the number of SPGD iterations, which is crucially related to the ultimate MD rate. However, the aforementioned method was based on the measurement of a near-field intensity pattern which would inevitably require an additional optical system such as a 4-f system like most other methods [10], [11], [12], [15], [16], [17], [18], [19], [20], [28]. Furthermore, it has yet to be confirmed whether or how well such a method can obtain the modal coefficients in real-time and real experimental environments, because no experiment was carried out based on it.

In this regard, we present an online real-time hybrid CNN/SPGD MD method based on the direct measurement of far-field intensity patterns of fiber modes. It is noteworthy that although this method uses the SPGD algorithm to finalize the MD after first obtaining the initial value of each mode's coefficient via the CNN as in Ref. [28], the following novel aspects are distinctively investigated and clarified in this article: (1) the hybrid CNN/SPGD algorithm is implemented to the MD based on the direct measurement of far-field intensity patterns of fiber modes, which plays a crucial role in improving the resultant correlation accuracy between the measured and reconstructed beams; (2) an online real-time MD based on the proposed method is experimentally demonstrated by a full-connectorized system, including a CCD camera and a computer, rather than going through a post process after simply storing the recorded frames in a computer when measured; (3) the number of fiber modes for the online real-time MD extends to 8, which is the largest in the case of the online real-time MD that has been

investigated to date to the best of our knowledge [10], [16], [18], [19], [22], [24].

The detailed outline of this article is given as follows: In Section II, the general procedure on how the linear-polarization (LP) modes of an MMF/LMAF are decomposed into free-space HGMs is briefly introduced (see Ref. [9] for more details), and the proposed hybrid MD method, which combines the CNN and the SPGD algorithm, implemented into the far-field intensity patterns of fiber modes is explained. In Sections III and IV, the numerical-only and full experimental results on the determination of the modal coefficients of the LP modes of a typical MMF/LMAF are presented and analyzed, respectively. In Section V, the practicality and effectiveness of the proposed method are discussed in view of an online real-time MD method for fiber-mode analysis, and the conclusions are drawn. In addition, throughout our whole discussions that follow, including both simulations and experiments, the MMF/LMAF under consideration has the V-parameter of 5.5 for 654-nm light, which supports 8 LP modes in total.

II. SIMULATION METHOD

A. Conversion of Linearly Polarization Mode to Hermite Gaussian Mode

The total field of a beam guided by an MMF/LMAF at the fiber end, i.e., at $z = 0$, is assumed to be represented by the superposition of normalized LP modes [9]:

$$E_{\text{Fiber}}(x, y) = \sum_{j=1}^N \rho_j \psi_j(x, y), \quad (1a)$$

with

$$\rho_j = |\rho_j| e^{i\phi_j}, \quad (1b)$$

where $\psi_j(x, y)$ denotes the j -th guided LP-mode field normalized as $\int_{-\infty}^{\infty} |\psi_j|^2 dx dy = 1$, $|\rho_j|^2$ is the j -th guided mode's relative power normalized as $\sum_j |\rho_j|^2 = 1$, ϕ_j the relative phase of the j -th guided mode to that of the fundamental guided mode (LP₀₁). Since the LP modes are the fiber modes guided in the given MMF/LMAF, they are not suitable basis modes for expressing far-field patterns [9]. Therefore, for considering the field propagation from the fiber's end into the free space, i.e., the air, each fiber mode should be converted into an appropriate set of free-space modes. That is, each LP mode is represented by the superposition of HGMs as follows [9], [26], [27]:

$$\xi_j(x, y, z) = \sum_{l,m} a_{j,l,m} F_{j,l,m}(x, y, z), \quad (2a)$$

with

$$a_{j,l,m} = \iint_{-\infty}^{\infty} \psi_j(x, y) F_{j,l,m}(x, y, 0) dx dy, \quad (2b)$$

where ξ_j and $F_{j,l,m}$ represent the converted free-space field function of the j -th guided mode and the corresponding eigen HGMs in the free space, respectively, in which the indices l and

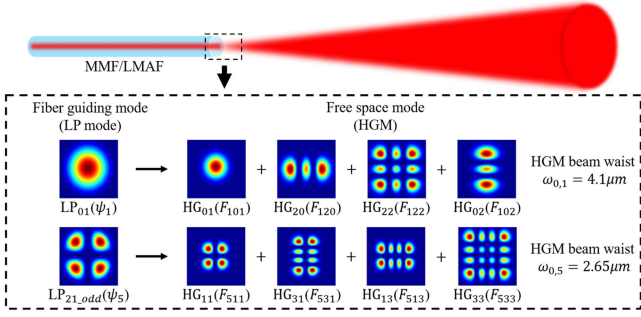


Fig. 1. Examples of MD of the LP modes to the free-space modes (HGMs). LP_{01} ($LP_{21,odd}$) mode is decomposed to the 4 different HGMs with corresponding beam waist $\omega_{0,1} = 4.1 \mu\text{m}$ ($\omega_{0,5} = 2.65 \mu\text{m}$). Refer to [9] for more details.

m indicate the order of the Hermite polynomial in the x and y directions, respectively. Their full expressions can be found in Ref. [9]. From the field-continuity condition at $z = 0$, the profiles of each LP mode and its corresponding superposition of HGMs must be equal at the fiber end, i.e., $\psi_j(x, y) = \xi_j(x, y, 0)$. It is noteworthy that $a_{j,l,m}$ is determined to be a real quantity because both $\psi_j(x, y)$ and $F_{j,l,m}(x, y, 0)$ can be set to be real fields at the fiber end [9]. Then, the coefficients $a_{j,l,m}$'s are determined by the values such that they make $\sum_{l,m} |a_{j,l,m}|^2$ become as close as 1 within a certain tolerance quantity (e.g., 0.01) while varying the beam waist $\omega_{0,j}$ of the corresponding HGMs (refer to Ref. [9] for more details).

Fig. 1 shows an example of the conversion between LP modes to the corresponding HGMs for the MMF/LMAF under consideration. ψ_1 corresponding to LP_{01} is represented by the superposition of 4 HGMs including HG_{01} among the HGM group with the beam waist $\omega_{0,1} = 4.1 \mu\text{m}$, and ψ_5 corresponding to $LP_{21,odd}$ is represented by the superposition of 4 HGMs including HG_{11} among the HGM group with $\omega_{0,5} = 2.65 \mu\text{m}$. The all the coefficients $a_{j,l,m}$'s found for the given LP modes (ψ_j) and HGMs ($F_{j,l,m}$) with the corresponding beam waist $\omega_{0,j}$ of each HGM group can be referred to Ref. [9]. In each LP mode, the total sum of $\sum_{l,m} |a_{j,l,m}|^2$ was obtained to be greater than 0.99.

After all, the total output beam pattern at a distance z from the fiber end can be written as the total sum of the product of ξ_j and the corresponding modal coefficient ρ_j as follows:

$$\begin{aligned} E_{\text{FS}}(x, y, z) &= \sum_j \rho_j \xi_j(x, y, z) \\ &= \sum_{j,l,m} |\rho_j| e^{i\phi_j} a_{j,l,m} F_{j,l,m}(x, y, z), \end{aligned} \quad (3)$$

where E_{FS} represents the far-field pattern of the total output beam in free space at a distance z from the fiber end. Note that the $\xi_j(x, y, z)$ can be regarded as an equivalent free-space mode field converted from the fiber-mode counterpart, i.e., $\psi_j(x, y)$. In fact, they become identical at the fiber end, i.e., $\psi_j(x, y) = \xi_j(x, y, 0)$. The quantities $|\rho_j|^2$ and ϕ_j denote the power fraction and the phase difference of the j -th LP mode as already

defined in (1b), respectively. It is noteworthy that all the quantities given in (3) are known except for the modal coefficients ρ_j 's. Therefore, they will be obtained through the MD procedure to be described in the sections that follow. Whilst the MD is carried out in terms of the "equivalent free-space modes" represented by $\xi_j(x, y, z)$'s, its outcome will be the solution to ρ_j 's.

In addition, when the far-field intensity patterns are measured experimentally, it is very important to identify where the origin of the corresponding HGMs is located with a high degree of accuracy. In this work, the iterative D4 σ technique that was devised in our previous work [9] is used to determine of the location of the origin of the HGMs from the measured far-field intensity patterns, which is, in fact, based on a simple iterative optimization procedure compensating the centroid mismatch between the measured and reconstructed far-field intensity patterns (refer to Ref. [9] for more details).

By the way, similar to the conjugate-pair issue in the near-field MD, there is a pair-beam-field issue in the far-field MD in that a pair of different phase combinations of LP modes can produce an identical far-field intensity pattern [17], [18], [23]. If the CNN is trained with far-field intensity patterns without considering the existence of the pair-beam field, it will undergo an ambiguity problem, thereby resulting in poor learning outcomes. Similar to the previous near-field MD, it is necessary to deal with or label the different phase combinations in an appropriate manner, so that they are treated as a single-valued parameter set [17], [18], [23]. In order to label them via an appropriate single-valued parameter set, the relationship between the phase difference ϕ_j of the original-beam field and the phase difference ϕ'_j of the pair-beam field for each LP mode should be clarified.

In (3), the total phase shift of a given far-field pattern related with an LP mode denoted by ψ_j is expressed as the sum of the phase difference ϕ_j and the additional phase shift $(l + m + 1)\zeta(z)$ of the corresponding HGMs denoted by $F_{j,l,m}(x, y, z)$ [9], and thus, the total phase-shift factor $\gamma(j, l, m)$ represented in a real quantity becomes

$$\gamma(j, l, m) = \cos[\phi_j + (l + m + 1)\zeta(z)], \quad (4a)$$

with

$$\zeta(z) = \text{atan}(z/z_0), \quad (4b)$$

where z_0 denotes the Rayleigh length. Note that the Rayleigh lengths of the LP modes supported with $V = 5.5$ are as small as just a few tens of micrometers, so that under far-field condition, $\zeta(z)$ is simply reduced to $\pi/2$. Thus, the second term in (4a) invariably becomes an integral multiple of $\pi/2$. Thus, the outcomes of the total phase factor $\gamma(j, l, m)$ can be divided into two difference cases, depending on whether $(l + m)$ is an even or odd number as follows:

$$\gamma(j, l, m) = \begin{cases} -\sin[\phi_j + n\pi], & \text{if } l + m = 2n, \\ \cos[\phi_j + (n + 1)\pi], & \text{if } l + m = 2n + 1, \end{cases} \quad (5)$$

where n denotes a non-negative integral number.

If one now supposes that there is a pair-beam field that produces the same far-field "intensity" pattern as the original-beam field does, its total phase-shift factor $\gamma'(j, l, m)$ should be the

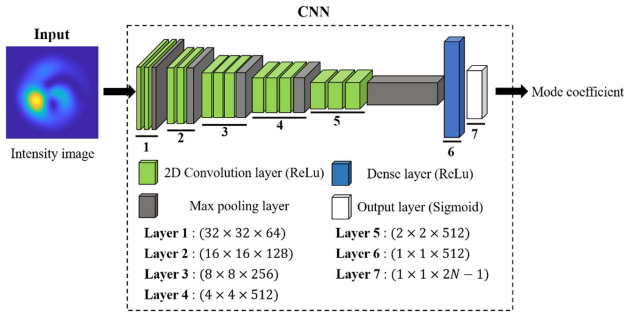


Fig. 2. Architecture of the CNN model for obtaining the modal coefficients from the intensity pattern.

negative of $\gamma(j, l, m)$, i.e., $\gamma'(j, l, m) = -\gamma(j, l, m)$, which is equivalent to the complex-conjugate relation between a pair of fields that result in the same intensity pattern at a distance if the fields are represented in complex quantities. This subsequently implies that the corresponding phase difference of the pair-beam field ϕ'_j should be given by

$$\phi'_j = \begin{cases} -\phi_j, & \text{if } l + m = 2n, \\ \pi - \phi_j, & \text{if } l + m = 2n + 1, \end{cases} \quad (6)$$

where n is a non-negative integral number. Intuitively, this consequence is obvious in that the other case, i.e., $\phi_j + \pi$, which just satisfies the given negative phase-shift-factor condition, cannot be taken as the proper phase difference of the pair-beam field, because phase difference ϕ_j is quantified relative to the initial phase of LP_{01} mode in the given formulation. Therefore, to eliminate the ambiguity in training the CNN incurred by the existence of a pair-beam field, one should deal with ϕ_j and ϕ'_j as a single-valued parameter set. In fact, this can readily be done if the phase difference ϕ_j is represented by its cosine or sine value depending on whether $(l + m)$ is an even or odd number, respectively, as follows:

$$\Phi_j = \begin{cases} \cos \phi_j, & \text{if } l + m = 2n, \\ \sin \phi_j, & \text{if } l + m = 2n + 1, \end{cases} \quad (7)$$

where n is a non-negative integral number. With this labelling, both ϕ_j and ϕ'_j are to be treated as a single-valued parameter set, thereby completely resolving the ambiguity problem in training the CNN, which can greatly help improve the overall accuracy of the CNN model.

B. Convolutional Neural Network Algorithm

In terms of reducing the MD rate, a CNN method definitely exhibits a significant advantage over iterative methods, such as the SPGD method [17], [18], [19], [20], [21], [22], [23], [24]. Notwithstanding, in order to maximize the benefit of a CNN method in view of the calculation time, it is important how to set its layers. If the number of the CNN layers is too small, the result may not converge, and conversely, if it is too large, the calculation time may become too long or overfitting of the training data may occur [28].

We here consider the VGG-16 model [17], which is slightly modified for MD as shown in Fig. 2. The CNN architecture consists of a total of 7 layers, and 3×3 kernel filters and 2×2

max-poolings are utilized in the 5 convolution layers. The activations of all of the convolution layers and fully connected layer 6 are set to the ReLU, which is commonly equipped as the activation in the hidden layer of the image recognition network [17], [29]. Also, the activation of the output layer is modified from the Softmax activation to the Sigmoid activation for matching the normalized modal coefficient.

As shown in Fig. 2, the single gray data of the far-field intensity pattern of the beam under consideration is used for the CNN input. In the process of pre-learning CNN, our CNN model is trained with the far-field intensity patterns formed by means of randomly generating the modal coefficients of $|\rho_j|$ and ϕ_j based on (3). If the size of the input image is too large, the capacity required for learning also becomes too large, thereby increasing the learning time. Therefore, a data size of (32×32) is used as the input image. For preserving the intensity pattern to the input, the largest value of the intensity distribution is set to 511, so that the intensity value of each pixel is normalized to be 0 to 511. The output vector of the CNN result is set to a total of $(2N - 1)$ values by adding the modal power fractions ($|\rho_1|^2, |\rho_2|^2, \dots, |\rho_N|^2$) of N modes and the phase differences (ϕ_2, \dots, ϕ_N) of $N - 1$ modes relative to LP_{01} . Since the Sigmoid activation is set as the output activation in the CNN, the phase difference ϕ_j is labeled to Φ_j by (7). For back propagation of the training system in CNN, the loss of the network is determined by the mean squared error (MSE) as follows:

$$\text{MSE}(\Delta) = \frac{1}{M} \sum_{i=1}^M \sum_{j=1}^{2N-1} (y_o^i[j] - y_d^i[j])^2, \quad (8)$$

where y_o and y_d represent the output vector of the CNN and the modal coefficient vector of the input beam, respectively; M is the total number of the training set. In the training procedure, 2 million samples of artificially generated data are used as the training set with a batch size of 64. Then, the stochastic gradient descent is selected for the optimizer, which updates the parameters of each layer during the training process.

C. Stochastic Parallel Gradient Descent Algorithm

The speed of an SPGD algorithm crucially depends on how closely to the global minimum the initial coefficients for optimization are chosen. That is, for MD, if the initial conditions were ill-determined, such as being set farther from the global minimum of the modal-coefficient solution, the decomposing time would increase, also having a higher chance of converging into a local minimum [9], [11]. Therefore, since it is important to set an appropriate initial condition for each modal coefficient, the initial condition for each modal coefficient is determined by the CNN model described in Section II-B. In order to compare the reconstructed beam image with the reference beam image during the SPGD algorithm, a cost function is calculated at a distance $z = L$ based on the correlation function as follows [9]:

$$C = 1 - \frac{\iint I_r(x, y) I_{FS}(x, y) dx dy}{\sqrt{\iint I_r^2(x, y) dx dy \iint I_{FS}^2(x, y) dx dy}}, \quad (9)$$

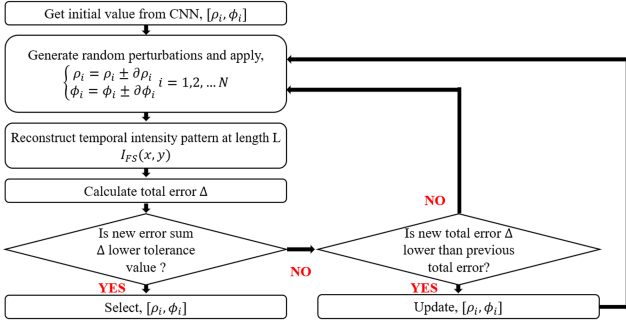


Fig. 3. Flow chart of the SPGD algorithm for obtaining the modal coefficients.

where the symbol I_r represents the ideal intensity pattern generated by the simulation via (3) or the intensity pattern measured by a CCD camera. I_{FS} represents the absolute squared value of the far-field pattern E_{FS} via (3), i.e., $I_{FS}(x, y) = |E_{FS}(x, y, L)|^2$. Fig. 3 summarizes the whole CNN/SPGD procedure. In our previous study [9], when the parameter set converged to a local minimum, a strong random perturbation was additionally applied to escape from it. However, if appropriate initial conditions are set by the CNN, the cost function C does not necessarily encounter such a local minimum issue. Thus, such an additional measure is excluded in this study.

III. SIMULATION RESULTS

A. Modal Decomposition Results by the Convolutional Neural Network With Various Outputs

The overfitting issue, which crucially degrades the accuracy of the CNN, can be prevented by letting the training set consist of a sufficiently large amount of data [28]. However, the procedure of training the CNN with such a large amount of data may require an excessive amount of RAM (random access memory) resources and increase the total training time. Since the low-resolution image data consumes a relatively less amount of RAM than the high-resolution image data, the CNN can be trained more effectively with a larger number of low-resolution image data than high-resolution image data even without increasing the size of RAM [12]. In this study, we consider resolving the overfitting issue by training the CNN with a large-capacity training set by reducing the resolution of the image data, as recently investigated in the sub-sampled MD [12]. In the training procedure, 2 million samples of data are set as the training data for all 3-, 6-, and 8-mode MD cases.

In addition to the impact by the size of the training set, it is important to control the learning rate (lr) and the number of epochs for training the CNN to obtain proper convergence of the MSE loss. In all MD cases, the CNN is trained until the MSE loss expressed by (8) becomes 3.0×10^{-4} or less. Also, the lr is adjusted at every 50 epochs such that the loss converges appropriately. After training the CNN with 110 epochs, the MSE loss Δ of 3-, 6-, and 8-mode MD cases are calculated to be 6.0×10^{-5} , 1.3×10^{-4} , and 2.6×10^{-4} , respectively. The resultant lr and the number of epochs with respect to the number of modes are summarized in Table I. In addition, the evolutions of the

TABLE I
SUMMARY OF THE CNN TRAINING

Mode #	1st train #	2nd train #	3rd train #	Total #
3	50 (lr=0.1)	50 (lr=0.05)	10 (lr=0.01)	110
6	50 (lr=0.1)	50 (lr=0.05)	10 (lr=0.01)	110
8	50 (lr=0.1)	50 (lr=0.05)	10 (lr=0.01)	110

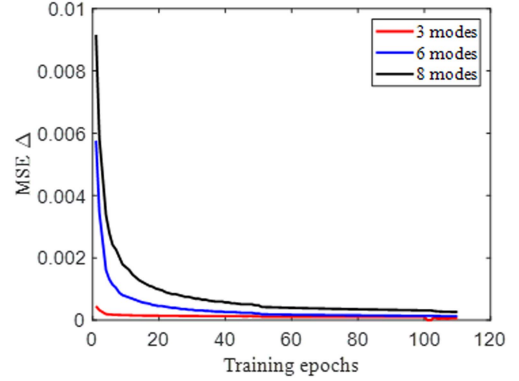


Fig. 4. Evolutions of the MSE loss for 3-, 6-, and 8-mode training process with respect to epochs. The MSE loss Δ given by (8) of 3-, 6-, and 8-mode cases are calculated to 6.0×10^{-5} , 1.3×10^{-4} , and 2.6×10^{-4} , respectively.

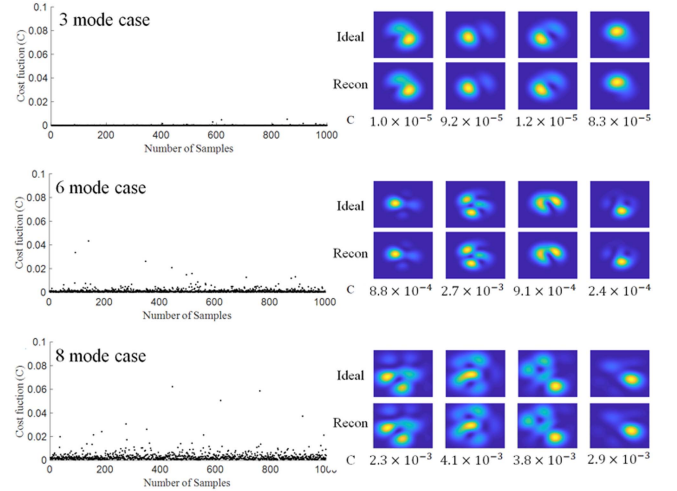


Fig. 5. CNN-based MD simulation results for 1000 samples. The cost function C values by (9) for 3-, 6-, and 8-mode MD cases are given by 4.7×10^{-5} , 1.4×10^{-3} , and 3.1×10^{-3} , respectively.

MSE loss with respect to the epochs of training are shown in Fig. 4.

To judge the accuracy of the trained CNN, the modal coefficients are acquired by introducing an arbitrarily generated intensity pattern into the CNN. Then, the intensity pattern of the beam is reconstructed based on the obtained modal coefficients, and the cost function C is calculated through (9) for all 3-, 6-, and 8-mode MD cases. 1000 intensity patterns are randomly generated, and the resultant cost function C obtained between the ideal beam pattern and the reconstructed beam pattern in each case is shown in Fig. 5. The mean values of the cost function C for the 3-, 6-, and 8-mode MD cases are given by 4.7×10^{-5} ,

TABLE II
MEAN DEVIATIONS OF THE MODAL POWER FRACTION OBTAINED AS A RESULT OF CNN-BASED MD OF 3-, 6-, AND 8-MODE CASES

	3-mode case	6-mode case	8-mode case
$\Delta \rho_{01} ^2$	1.36×10^{-3}	4.58×10^{-3}	5.62×10^{-3}
$\Delta \rho_{11,odd} ^2$	1.37×10^{-3}	5.69×10^{-3}	7.49×10^{-3}
$\Delta \rho_{11,even} ^2$	1.38×10^{-3}	5.37×10^{-3}	7.61×10^{-3}
$\Delta \rho_{02} ^2$	-	5.37×10^{-3}	6.25×10^{-3}
$\Delta \rho_{21,odd} ^2$	-	5.36×10^{-3}	7.21×10^{-3}
$\Delta \rho_{21,even} ^2$	-	5.05×10^{-3}	8.10×10^{-3}
$\Delta \rho_{31,odd} ^2$	-	-	5.40×10^{-3}
$\Delta \rho_{31,even} ^2$	-	-	5.06×10^{-3}

TABLE III
MEAN DEVIATIONS OF THE MODAL PHASE DIFFERENCE OBTAINED AS A RESULT OF CNN-BASED MD OF 3-, 6-, AND 8-MODE CASES

	3-mode case	6-mode case	8-mode case
$\Delta \phi_{11,odd} $	1.66×10^{-3}	8.18×10^{-3}	1.15×10^{-2}
$\Delta \phi_{11,even} $	1.71×10^{-3}	8.28×10^{-3}	1.23×10^{-2}
$\Delta \phi_{02} $	-	7.35×10^{-3}	1.11×10^{-2}
$\Delta \phi_{21,odd} $	-	8.52×10^{-3}	1.34×10^{-2}
$\Delta \phi_{21,even} $	-	8.47×10^{-3}	1.26×10^{-2}
$\Delta \phi_{31,odd} $	-	-	1.17×10^{-2}
$\Delta \phi_{31,even} $	-	-	1.22×10^{-2}

1.4×10^{-3} , and 3.1×10^{-3} , respectively. As observed in the previous reports [18], [19], [22], [24], the CNN-based MD efficiency tends to decrease considerably when the total number of modes for MD is increased to 8 modes.

In addition, the MD results are analyzed by calculating the mean deviations of the modal power fractions and phase differences of the reconstructed beam from those of the ideal beam as follows:

$$\Delta |\rho_j|^2 = \left| |\rho_{j,ideal}|^2 - |\rho_{j,reconst}|^2 \right|, \quad (10a)$$

$$\Delta |\phi_j| = |\phi_{j,ideal} - \phi_{j,reconst}| / 2\pi, \quad (10b)$$

where $|\rho_{j,ideal}/reconst|^2$ and $\phi_{j,ideal}/reconst$ denote the j -th mode's modal power fraction and phase difference for the ideal or reconstructed beam, respectively. Note that the maximum modal power fraction is already normalized to unity. The resultant mean deviations of the modal power fractions and phase differences for the whole 1000 samples are summarized in Table II and Table III, respectively. In fact, the CNN-based MD results reflect the same trends as observed in the previous reports [17], [22], [24]. That is, the deviations increase with the number of modes considered for MD [22], [24]. This feature becomes more significant when the total number of modes for MD is increased to 8 modes. Thus, to alleviate this typical feature the

CNN-based MD, a special additional measure is required to be taken.

B. Modal Decomposition Results by the Hybrid Method

When obtaining the modal coefficients of up to 6 modes, the CNN-based MD considered in the previous section may be regarded sufficient. However, we could see that its efficiency dropped significantly in the 8-mode case. In this case, we can think of improving the accuracy of the MD result by additionally performing the SPGD-based MD once the initial condition has firstly been set through the CNN. In practice, it is difficult to increase the correlation between the measured beam and the reconstructed beam over 0.999, since the intensity noise generated in the CCD distorts the beam image in the experimental environment where the intensity noise level is typically as high as -30 dB [13], [15], [30]. Therefore, it is sensible to run the additional SPGD process until the cost function C between the randomly generated ideal beam and the reconstructed beam decreases to less than to a certain tolerance value, i.e., 0.001, for example. Moreover, to keep the overall simulation time within a reasonable range, it is also sensible not to run the additional SPGD process over a certain maximum number of iterations, i.e., 400, for example, even when the cost function C does not achieve 0.001 or less. These two strategies should be useful and effective for realizing a real-time MD system which is allowed to work with an acceptable tolerance on the accuracy [9], [11].

The CNN-based MD method obtains the modal coefficients by inputting randomly generated beam patterns into the trained CNN as explained in Section II-B. In the SPGD-based MD method, the initial modal coefficients are randomly set and optimized through the SPGD algorithm as explained in Section II-C. In the case of the hybrid CNN/SPGD-based MD method, the initial modal coefficients are firstly obtained by the trained CNN rather than randomly set. Those modal coefficients pre-processed by the trained CNN are further optimized through the SPGD algorithm. In the following, in order to make fair comparison with the previous CNN-based MD results [17], [18], [19], [20], [21], [22], [23], [24], we consider trying a test set consisting of 1000 randomly generated different image samples with them, and characterize their performance parameters in terms of their mean values. The test set can be regarded as a pre-recorded data set, so that both CNN processes undertaken during the CNN-based MD and the hybrid CNN/SPGD-based MD are carried out by parallel computing. On the contrary, both SPGD processes undertaken during the SPGD-based MD and the hybrid CNN/SPGD-based MD are carried out by sequential computing.

Fig. 6 shows a series of MD results obtained by the CNN-, SPGD-, and hybrid CNN/SPGD-based MD methods, respectively, as described above. As can be seen in Fig. 6(a), the cost function C of the hybrid CNN/SPGD MD result is significantly lower than those of the other two methods. In fact, their mean values are given by 3.1×10^{-3} , 7.8×10^{-2} , and 6.6×10^{-4} for the CNN-, SPGD-, and hybrid CNN/SPGD-based MD methods, respectively. This implies that the accuracy of the hybrid CNN/SPGD MD method is about 20 times higher than those

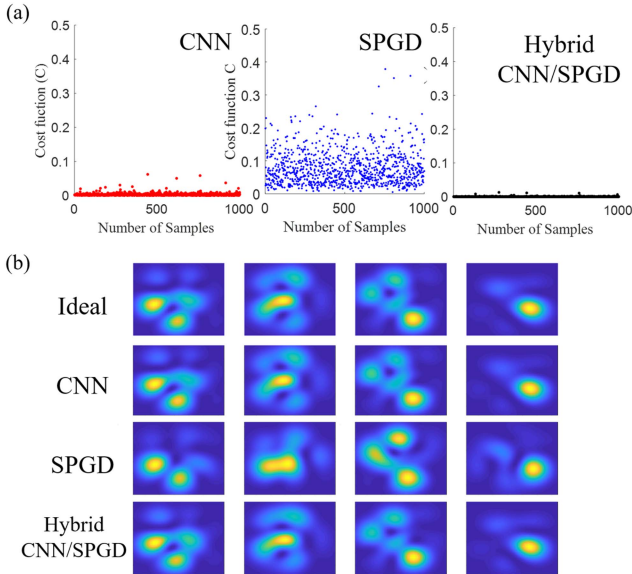


Fig. 6. Simulation results by the CNN-, SPGD-, and hybrid CNN/SPGD-based MD methods. (a) The cost function C by (9) obtained as a result of each MD for 1000 samples. The mean cost function C of the CNN-, SPGD-, and hybrid CNN/SPGD-based MD results are given by 3.1×10^{-3} , 7.8×10^{-2} , and 7.0×10^{-4} , respectively. (b) Intensity patterns of the ideal beam and the reconstructed beam generated by the modal coefficients obtained by each MD method.

of the other two. In Fig. 6(b), some typical examples of the reconstructed beam intensity patterns by the three different MD methods are illustrated in comparison with the ideal beam intensity patterns. In fact, one can readily see that the hybrid CNN/SPGD-based MD results outperform those by the other two.

In Table IV, the MD performance parameters of the three MD methods are summarized, which include the mean deviations of the modal power fraction and phase difference, the correlation accuracy, and the decomposing time measured by a personal computer. Whilst the cost function C values of the CNN- and SPGD-based MD results are similar to each other, the mean deviations of the modal power fraction and phase difference of the latter are significantly larger than those of the former. This is due to the fact that the SPGD-based MD tends to find a local minimum point when initially ill-conditioned unless a special measure is taken to avoid such a situation. In fact, one can readily see that the hybrid CNN/SPGD MD method outperforms the other two in every parameter except for the decomposing time. An intriguing point that one can find in terms of the decomposing time, is that the hybrid CNN/SPGD MD takes significantly less than the SPGD-only MD although the former goes through both the CNN process and the SPGD process. This is thanks to the fact that the initial conditions for the SPGD process are well determined by the CNN process. This consequence, in turn, brings in not only shortening the decomposing time in comparison with the SPGD-only MD, but also improving the correlation accuracy in the comparison with the CNN-only MD.

Whilst the CNN-based MD for a test set of 1000 image samples takes the shortest decomposing time, this feature should be meaningful only when pre-recorded image data are available,

TABLE IV
MEAN DEVIATIONS OF MODAL COEFFICIENTS OBTAINED BY EACH MD METHOD AND THE AVERAGES OF DECOMPOSING TIME AND C VALUE

	CNN	SPGD	Hybrid
$\Delta \rho_{01} ^2$	5.62×10^{-3}	8.76×10^{-2}	5.22×10^{-3}
$\Delta \rho_{11,odd} ^2$	7.49×10^{-3}	8.78×10^{-2}	6.97×10^{-3}
$\Delta \rho_{11,even} ^2$	7.61×10^{-3}	8.72×10^{-2}	7.01×10^{-3}
$\Delta \rho_{02} ^2$	6.25×10^{-3}	9.62×10^{-2}	6.17×10^{-3}
$\Delta \rho_{21,odd} ^2$	7.21×10^{-3}	9.38×10^{-2}	6.82×10^{-3}
$\Delta \rho_{21,even} ^2$	8.10×10^{-3}	9.19×10^{-2}	7.70×10^{-3}
$\Delta \rho_{31,odd} ^2$	5.40×10^{-3}	7.80×10^{-2}	5.31×10^{-3}
$\Delta \rho_{31,even} ^2$	5.06×10^{-3}	7.65×10^{-2}	5.16×10^{-3}
$\Delta \phi_{11,odd} $	1.15×10^{-2}	33.3×10^{-2}	9.85×10^{-3}
$\Delta \phi_{11,even} $	1.23×10^{-2}	32.8×10^{-2}	1.04×10^{-2}
$\Delta \phi_{02} $	1.11×10^{-2}	35.2×10^{-2}	9.50×10^{-3}
$\Delta \phi_{21,odd} $	1.34×10^{-2}	36.5×10^{-2}	1.09×10^{-2}
$\Delta \phi_{21,even} $	1.26×10^{-2}	33.7×10^{-2}	1.09×10^{-2}
$\Delta \phi_{31,odd} $	1.17×10^{-2}	36.0×10^{-2}	1.04×10^{-2}
$\Delta \phi_{31,even} $	1.22×10^{-2}	34.9×10^{-2}	1.03×10^{-2}
$t_{Average}$	3.35 ms	66.2 ms	30.9 ms
$C_{Average}$	3.1×10^{-3}	7.8×10^{-2}	6.6×10^{-4}

so that parallel computing is applicable to them. Thus, in the case when the online real-time MD is performed for an individual beam image, such a merit of the CNN-based MD will fade out. The characteristics of the convergence time of the three different MD methods will be discussed in more detail in the section that follows, in which the two different MD methods are implemented in online real-time forms. In addition, since the convergence times given in Table IV were actually measured by a simple personal computer, there is much room for improvement in reducing them if even faster a computing system is instead utilized.

IV. EXPERIMENT RESULTS

The experimental setup to demonstrate the proposed hybrid CNN/SPGD MD based on the measurement data obtained from a CCD camera is shown in Fig. 7. As in our previous investigation [9], a laser with a central wavelength of 654 nm and a bandwidth of 0.9 nm and SMF-28 are used as the source and the MMF/LMAF under consideration, respectively. Note that SMF-28 has a step-index core with 8.2 μm diameter and an NA of 0.14, thereby resulting in the V-number of 5.5. Thus, it eventually supports 8 LP modes in total for 654-nm light. In addition, to ensure the excitation of LP modes, the incident light is collimated through a polarizing beam splitter, so that only linearly polarized light is incident on the MMF/LMAF under consideration. The CCD camera is placed at a distance of 20 mm from the end of the MMF/LMAF under consideration, which is distant enough for ensuring that the measured field-intensity

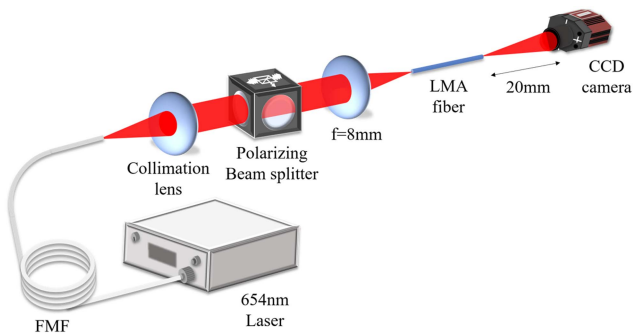


Fig. 7. Experiment setup for measuring the far-field intensity profiles. LMA: Large mode fiber (SMF-28); FMF: Few-mode fiber.

patterns are regarded as those of far-fields (note that the Rayleigh length of F_{00} mode converted from LP_{01} mode under the given condition is determined by $z_0 = 31 \mu\text{m}$) [31] as well as being sufficiently large relative to the resolution of the CCD camera used (unit pixel size: $4.54 \times 4.54 \mu\text{m}^2$) [9].

For making the measured images of 2752×2192 pixels suitable to the CNN, they are cropped and resized to images of 32×32 pixels. In Section IV-A, the results of the CNN-based MD and the hybrid CNN/SPGD MD are first compared by using the recorded far-field intensity patterns. In Section IV-B, the online real-time MD is eventually investigated, in which the MD is performed in real-time as soon as the beam image is acquired by the CCD camera.

A. Modal Decomposition Results by the Hybrid Method With Recorded Data of the Measured Images

Using the experimental setup shown in Fig. 7, the operation of the hybrid CNN/SPGD-based MD is investigated with the real beam patterns measured by the CCD camera. In total, 200 beam images are recorded. In fact, the far-field patterns are measured and recorded for 10 different mode-excitation conditions and in each condition 20 frames of image data are taken by the CCD camera. With them, the CNN-based MD and the hybrid CNN/SPGD-based MD are performed and their characteristics are analyzed. In result, the total elapsed times for the former and the latter were given by 2.45 s and 14.21 s, respectively, so that the decomposing time for a single-frame beam pattern is calculated to be 12 ms and 71 ms, respectively.

Fig. 8 illustrates the experimental results obtained when the CNN-based MD and the hybrid CNN/SPGD-based MD were performed onto the measured beam patterns. Each curve shown in Fig. 8(a) represents the cost function C calculated between the measured and reconstructed beam patterns using the modal coefficients obtained as a result of each MD method. After setting the modal coefficients obtained by the CNN as an initial condition for each frame, the cost function C significantly decreased when the SPGD process was performed 400 times as described in Section III-B. In addition, the mean C value for the 200 frames is calculated to be 0.0369 and 0.0087 for the CNN-based MD and the hybrid CNN/SPGD-based MD, respectively. Fig. 8(b) shows the reconstructed beam patterns and the C values obtained by both MD methods when they have the lowest C values for

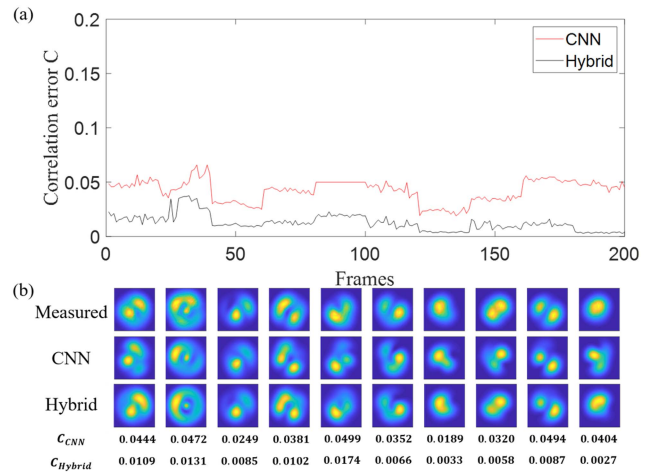


Fig. 8. Experimental results with the recorded frames. (a) Evolution of the cost function C between the measured beam and the reconstructed beam for every frame. (b) Experimental measurements and the corresponding numerical reconstructions based on the CNN and the hybrid MD results. The corresponding C values are depicted below and the average C values of CNN MD and the hybrid MD are 0.0369 and 0.0087, respectively.

the 10 different beam-pattern conditions. In all cases except for one beam-pattern condition, the accuracy increases more than twice. In fact, the reconstructed beam patterns all show great similarity to the measured beam patterns.

B. Online Real-Time Measured Data Modal Decomposition

In order to analyze the dynamic aspects of HOMs temporarily varying in the optical fiber, the MD should be obtained in real-time. We here investigate the proposed hybrid CNN/SPGD-based MD method for its characteristics as an online real-time MD method, which should be able to acquire the modal coefficients in real-time through a single beam pattern measured by the CCD camera. In the online real-time MD process, the exposure time of the CCD camera was set to 10 ms, and the modal coefficients were obtained in real-time by the proposed hybrid CNN/SPGD-based MD for every frame of the measured beam patterns. The decomposing time of the online real-time hybrid CNN/SPGD-based MD was measured to be 495.6 ms on average. The video image of the online real-time hybrid MD is presented in Visualization 1. The cost function C is calculated to be 0.0154 on average, which implies this MD result is more than twice as good as the CNN-based MD experimental results previously reported to date [18], [19], [22], [24]. In fact, the proposed hybrid CNN/SPGD-based MD can effectively operate under the online real-time condition with a rate of the inverse of the decomposing time of 495.4 ms, i.e., with ~ 2 Hz. By the way, in the case of the CNN-based MD with recorded measured data, which was discussed in Section IV-A, the decomposing time for a single frame was calculated to be 12 ms. However, it was elongated to ~ 262 ms under the online real-time condition. This implies that the most time-consuming part in the online real-time hybrid CNN/SPGD-based MD was the part for obtaining the initial modal coefficients through the CNN. This consequence can be explained in two folds: One is that the CNN process is

normally carried out via the graphics processing unit (GPU), which is greatly effective particularly for parallel computing, not for single-data or sequential computing. As a result, the decomposing time per unit frame image for the CNN-based MD increases if it is implemented into a sequentially measured data, which is the case of the online real-time MD. The other is that the data conversion time also considerably increases the overall decomposing time: In general, the beam pattern data measured by the CCD camera is stored in NumPy type and converted to Tensor type for GPU processing in the CNN. Then, the modal coefficients in Tensor type obtained as the outcome of the CNN must be converted back into NumPy type. It is well known that these data type conversion procedures consume a considerable amount of computing time.

V. CONCLUSION

In order to overcome both the accuracy issue of the CNN-based MD method and the local minimum issue of the SPGD MD method, we have investigated a hybrid method for MD of an LMA fiber that acquires the initial condition of the modal coefficients with the CNN and improves the accuracy through the SPGD. The direct far-field measurement method was also implemented to resolve the beam distortion issue caused by the auxiliary 4-f system that may also increase the overall system complexity [25]. For describing the beam propagation in free space from the fiber end, the far-field pattern of each LP mode is obtained by decomposing each fiber mode into HGMs. The proposed hybrid method has been proven effective both numerically and experimentally. In the numerical simulation, the CNN-based MD and the SPGD-based MD achieved the correlation errors, i.e., the C values, between the ideal and reconstructed beams of 3.1×10^{-3} and 7.8×10^{-2} , respectively. In contrast, the proposed hybrid CNN/SPGD MD obtained the C value of 6.6×10^{-4} , which, in fact, is over 20 times more accurate than the other two MD methods. In the experimental demonstration, the CNN-based MD method and the hybrid CNN/SPGD MD method obtained the C values of 0.0369 and 0.0087, respectively. The accuracy of the latter was more than four times as high as that of the former. However, in comparison with our own previous experimental results [9], the C value obtained from this work was rather large although there has been a huge improvement in term of MD rate. This is presumed to be due mainly to the limiting of the SPGD iteration number and the cropping and resizing of the measured images as described in Section IV, so that it is considered that a further improvement in the C value can be obtained by adjusting and optimizing those parameters [9], [23]. As for decomposing rates when performing MD using more than 1000 recorded images, the CNN-based MD method showed a decomposing rate of ~ 256 Hz whilst the hybrid CNN/SPGD MD method showed a decomposing rate of ~ 20 Hz, which was mainly because of the merit of the parallel computing by GPU. However, when they were implemented in the online real-time format, they exhibited no big difference in terms of the decomposing rate, showing ~ 4 Hz and ~ 2 Hz, respectively. In fact, the more time consumption in the online real-time MD was due to the fact that the merit of parallel computing was no longer

exploited for the sequentially processed CNN and the repeated conversion of the data types consumed excessive computing times for the CNN. In addition, similar to the conventional near-field MD, a pair-beam field issue remains even in the far-field MD as long as the field-intensity patterns are measured at a single distance. Nevertheless, it has been shown that the ambiguity problem that may happen in the CNN owing to the pair-beam field issue can be resolved by properly labelling the phase differences with a single-valued parameter set in consideration of the mode-order indices. Moreover, the pair-beam field issue can completely be resolved with the far-field MD if the measurement of the field-intensity patterns is carried out at multiple distances as reported in Ref. [9], which can be realized in a rather straightforward manner in that the far-field MD does not require any auxiliary 4-f system. It is expected that the proposed and demonstrated hybrid CNN/SPGD MD method along with the direct far-field measurement procedure will be efficiently utilized in characterizing and analyzing complex modes formed in various LMA fibers.

REFERENCES

- [1] Y. Jeong, J. Sahu, D. Payne, and J. Nilsson, "Ytterbium-doped large-core fiber laser with 1.36 kW continuous-wave output power," *Opt. Exp.*, vol. 12, no. 25, pp. 6088–6092, 2004.
- [2] N. Broderick, H. Offerhaus, D. Richardson, R. Sammut, J. Caplen, and L. Dong, "Large mode area fibers for high power applications," *Opt. Fiber Technol.*, vol. 5, no. 2, pp. 185–196, 1999.
- [3] G. Oh, E. Chung, and S. H. Yun, "Optical fibers for high-resolution in vivo microendoscopic fluorescence imaging," *Opt. Fiber Technol.*, vol. 19, no. 6, pp. 760–771, 2013.
- [4] W. H. Renninger and F. W. Wise, "Optical solitons in graded-index multimode fibres," *Nature Commun.*, vol. 4, no. 1, pp. 1–6, 2013.
- [5] A. V. Smith and J. J. Smith, "Mode instability in high power fiber amplifiers," *Opt. Exp.*, vol. 19, no. 11, pp. 10180–10192, 2011.
- [6] H. Lü, P. Zhou, X. Wang, and Z. Jiang, "General analysis of the mode interaction in multimode active fiber," *Opt. Exp.*, vol. 20, no. 6, pp. 6456–6471, 2012.
- [7] D. B. S. Soh, J. Nilsson, S. Baek, C. Codemard, Y. Jeong, and V. Philippov, "Modal power decomposition of beam intensity profiles into linearly polarized modes of multimode optical fibers," *J. Opt. Soc. Amer. A*, vol. 21, no. 7, pp. 1241–1250, 2004.
- [8] J. W. Nicholson, A. D. Yablon, J. M. Fini, and M. D. Mermelstein, "Measuring the modal content of large-mode-area fibers," *IEEE J. Sel. Topics Quantum Electron.*, vol. 15, no. 1, pp. 61–70, Jan. 2009.
- [9] B. Kim, J. Na, J. Kim, H. Kim, and Y. Jeong, "Modal decomposition of fiber modes based on direct far-field measurements at two different distances with a multi-variable optimization algorithm," *Opt. Exp.*, vol. 29, no. 14, pp. 21502–21520, 2021.
- [10] L. Huang, S. Guo, J. Leng, H. Lü, and P. Zhou, "Real-time mode decomposition for few-mode fiber based on numerical method," *Opt. Exp.*, vol. 23, no. 4, pp. 4620–4629, 2015.
- [11] K. Choi and C. Jun, "High-precision modal decomposition of laser beams based on globally optimized SPGD algorithm," *IEEE Photon. J.*, vol. 11, no. 5, Oct. 2019, Art. no. 7103110.
- [12] K. Choi and C. Jun, "Sub-sampled modal decomposition in few-mode fibers," *Opt. Exp.*, vol. 29, no. 20, pp. 32670–32681, 2021.
- [13] K. Singh, P. Sharma, A. Dixit, B. Srinivasan, R. D. Koilpillai, and D. Venkitesh, "Theoretical and experimental investigation of the sources of error in stochastic parallel gradient descent-based digital modal decomposition technique," *Opt. Soc. Amer. Continuum*, vol. 4, no. 7, pp. 1916–1932, 2021.
- [14] L. Li, J. Leng, P. Zhou, and J. Chen, "Multimode fiber modal decomposition based on hybrid genetic global optimization algorithm," *Opt. Exp.*, vol. 25, no. 17, pp. 19680–19690, 2017.
- [15] E. S. Manuylovich, V. V. Dvoyrin, and S. K. Turitsyn, "Fast mode decomposition in few-mode fibers," *Nature Commun.*, vol. 11, no. 1, pp. 1–9, 2020.

- [16] E. Manuylovich, A. Donodin, and S. Turitsyn, "Intensity-only-measurement mode decomposition in few-mode fibers," *Opt. Exp.*, vol. 29, no. 22, pp. 36769–36783, 2021.
- [17] Y. An, L. Huang, J. Li, J. Leng, L. Yang, and P. Zhou, "Learning to decompose the modes in few-mode fibers with deep convolutional neural network," *Opt. Exp.*, vol. 27, no. 7, pp. 10127–10137, 2019.
- [18] Y. An, L. Huang, J. Li, J. Leng, L. Yang, and P. Zhou, "Deep learning-based real-time mode decomposition for multimode fibers," *IEEE J. Sel. Topics Quantum Electron.*, vol. 26, no. 4, Jul./Aug. 2020, Art. no. 4400806.
- [19] H. Gao, Z. Chen, Y.-X. Zhang, W.-G. Zhang, H.-F. Hu, and T.-Y. Yan, "Rapid mode decomposition of few-mode fiber by artificial neural network," *J. Lightw. Technol.*, vol. 39, no. 19, pp. 6294–6300, Oct. 2021.
- [20] Y. An et al., "Numerical mode decomposition for multimode fiber: From multi-variable optimization to deep learning," *Opt. Fiber Technol.*, vol. 52, 2019, Art. no. 101960.
- [21] H. Kim, "Convolution neural network based mode decomposition for degenerated modes via multiple images from polarizers," 2022, *arXiv:2207.03489*.
- [22] M. Jiang et al., "Deep mode decomposition: Real-time mode decomposition of multimode fibers based on unsupervised learning," *IEEE J. Sel. Topics Quantum Electron.*, vol. 28, no. 4, Jul./Aug. 2022, Art. no. 0900207.
- [23] S. Rothe, Q. Zhang, N. Koukourakis, and J. Czarske, "Intensity-only mode decomposition on multimode fibers using a densely connected convolutional network," *J. Lightw. Technol.*, vol. 39, no. 6, pp. 1672–1679, Mar. 2021.
- [24] Q. Zhang, S. Rothe, N. Koukourakis, and J. Czarske, "Learning the matrix of few-mode fibers for high-fidelity spatial mode transmission," *Appl. Phys. Lett. Photon.*, vol. 7, no. 6, 2022, Art. no. 066104.
- [25] J. Jahns and S. J. Walker, "Imaging with planar optical systems," *Opt. Commun.*, vol. 76, no. 5/6, pp. 313–317, 1990.
- [26] R. Brünig, Y. Zhang, M. McLaren, M. Duparré, and A. Forbes, "Overlap relation between free-space Laguerre Gaussian modes and step-index fiber modes," *J. Opt. Soc. Amer. A*, vol. 32, no. 9, pp. 1678–1682, 2015.
- [27] B. M. Heffernan, R. D. Niederriter, M. E. Siemens, and J. T. Gopinath, "Tunable higher-order orbital angular momentum using polarization-maintaining fiber," *Opt. Lett.*, vol. 42, no. 14, pp. 2683–2686, 2017.
- [28] F. Chen, "Modal decomposition of an incoherent combined laser beam based on the combination of residual networks and a stochastic parallel gradient descent algorithm," *Appl. Opt.*, vol. 61, no. 14, pp. 4120–4131, 2022.
- [29] K. Simonyan and A. Zisserman, "Very deep convolutional networks for large-scale image recognition," 2014, *arXiv:1409.1556*.
- [30] K. Choi, Y. Kim, Y. Yun, Y.-C. Noh, and C. Jun, "Study on factors degrading the accuracy of real beam modal decomposition," *Curr. Opt. Photon.*, vol. 5, no. 2, pp. 93–100, 2021.
- [31] E. Hecht, *Optics*. London, U.K.: Pearson, 2012.